Hindawi
Geofluids
Volume 2022, Article ID 9325958, 17 pages
https://doi.org/10.1155/2022/9325958

Research Article

Experimental Study on Compaction Characteristics and Mechanical Behavior of Crushed Rock Masses

Xiaolou Chi,[1] **Qiang Fu**,[1] **and Ke Yang**[1,2]

[1]*State Key Laboratory of Mining Response and Disaster Prevention and Control in Deep Coal Mines, Anhui University of Science and Technology, Huainan, Anhui 232001, China*
[2]*Institute of Energy, Hefei Comprehensive National Science Center, Hefei, Anhui 230031, China*

Correspondence should be addressed to Qiang Fu; fqymc@aust.edu.cn

Received 7 April 2022; Accepted 21 June 2022; Published 15 July 2022

Academic Editor: Dongjiang Pan

The compaction and consolidation process of a regenerated roof can be divided into two stages, namely, secondary fragmentation of crushed rock masses and pore structure adjustment. Therefore, the mechanical properties of the regenerated roof differs significantly from those of the primary roof. We performed confined compression tests of crushed mudstones and sandy mudstones using a self-developed compression testing apparatus. We studied the influence of the moisture content, compression ratio, particle size, and volume-based degradation on the compression and consolidation characteristics based on the microscopic morphology of the crushed rock masses. Further, the degrees of influence of these factors on the stability of the consolidated bodies were determined. Therefore, the influence mechanism of each factor on the compressive and shear strengths of the consolidated bodies was revealed. The results indicated that the compaction and consolidation of the crushed rock masses involved a constant adjustment of the contact and stress states of the rock masses. Under uniaxial compression and shearing, the consolidated bodies presented the features of ductile failure. The compression ratio and particle size were the most important influencing factors in the compressive and shear strengths of the consolidated bodies. Further, we carried out an orthogonal experiment and built a multivariate nonlinear regression model to quantitatively characterize the combined influence of these factors on the compaction characteristics of the crushed rock masses and the mechanical behavior of the consolidated bodies.

1. Introduction

During gangue filling mining and the slice mining of thick coal seams, crushed rock masses are gradually compacted to form consolidated bodies with a certain strength due to loading by the overlying strata or due to mechanical vibration. The degrees of compaction and consolidation of the rock masses have a direct bearing on the strengths of the consolidated bodies. The latter is considered a prerequisite for the safe recovery of coal pillars under railway tracks, water bodies, and buildings [1–4]. Therefore, studying the compaction characteristics of rock masses under different influencing factors and determining the consolidation strength and mechanical behavior of the consolidated bodies are important topics for investigation by scientists and engineers.

Over the years, much research has been conducted on the compression and consolidation characteristics of crushed rock masses under the influence of various factors [5–10]. Zhang et al. [11] proposed a fractal model for gangue compaction and fragmentation and examined the fractal features of crushed rock masses during compaction. Pappas and Mark [12] discussed the compaction characteristics of collapsed rock masses in the goaf. They obtained the relationship connecting the tangent modulus, secant modulus, and stress during rock block compaction, while Terzaghi's and Salamon's equations were used to describe the stress-strain relationship. Ma et al. [13] determined the compaction characteristics of limestone particles using the MTS815.02 electrohydraulic servo rock test system and the self-developed compression testing apparatus. They estimated the influence of the particle size distribution on the porosity during compaction. Bing-nan and Ai-guo

[14] designed compression tests for rock masses having different particle sizes and compression ratios. They further derived the stress-time curve for the entire compression process and revealed the influence mechanism of rock gradation on filling mining. Huang et al. [15] designed a triaxial compression test for rock masses and found that as the confining pressure increased, the bearing capacity of the rock masses also increased. Guo et al. [16] employed a resistivity tester for the stepwise compression testing of rock masses. They characterized the internal damage to the filling body at the hardening stage. Meng et al. [17] chose PTH as the filler in the creep model that is based on the creep compaction test for rock filling material. They further built a rheological model for the roof in solid filling mining. Su et al. [18] designed a group of compression tests for rock masses with different particle sizes and strengths. They found that the bulking factor of the rock masses at different stages of compaction was correlated logarithmically to the particle size. Zhan et al. [19] performed a numerical simulation using PFC and built a particle flow model for triaxial compression. Additionally, confined compression tests were performed for rock masses of different sizes. Bang-yong et al. [20] designed compression tests for saturated mudstones with different particle sizes and also derived an expression that relates the compaction stress and compressive modulus of the rock masses. Ma et al. [21] performed creep tests for saturated mudstones with different particle sizes. They found that the porosity of the rock masses had a negative exponential relationship with the creep time. The changes in porosity could be further divided into several distinct stages. Zhang et al. [22] used a self-developed deformation testing system for crushed rock masses with a large particle size under pressure (internal diameter 400 mm) to investigate their deformation characteristics. Zhenquan et al. [23] believed that the compaction of rock masses was progressive and involved the crushing, compaction, recrushing, and recompaction steps. This process can be roughly divided into two stages, namely, the crushing-compaction stage and the consolidation-compaction stage. Zhennan et al. [24] found that as the crushed rock masses were being compacted, the crushing rate was higher when the relative pressure was 0.5–0.6. Beyond this range, the crushing rate of the rock masses decreased, and the gradation of the rock masses tended to become stable. The gradation curve after crushing could be described using a quadratic polynomial. Xiao et al. [25] and Yimin et al. [26] reported that the crushing rate of the crushed rock masses under true triaxial compression increased along with the intermediate principal stress ratio. Wang et al. [27] estimated the deformation and energy dissipation characteristics of the rock masses during compression through experiments. Li et al. [28] conducted a series of compression tests for rocks as fillers with different gradations. They determined the relationship between the modulus of deformation and the degree of compression under stress. Cheng et al. [29] considered the influence of lateral pressure, degree of saturation, and particle size degradation on the stress vs. compression relationship of the solid fillers. Their experiments showed that the moisture content of rock masses in their natural state has little impact on the strengths of the rocks as fillers. Mingli [30] used the contact bond model in PFC3D to study the compaction stress and deformation pattern of rock masses with different gradations. Huaiting et al. [31] applied the clump model in PFC to generate irregular convex polyhedrons that simulated the gangue masses. On this basis, they studied the macroscopic mechanical responses and microscopic movement characteristics of gangues under triaxial compression. Shugang et al. [32] carried out compression tests for rock masses with different particle sizes and reinforced by different methods. Subsequently, they built a mechanical model for the rock masses as load-bearing bodies. De-fu et al. [33] proposed a method for building a 3D compression model for rock masses using the 3D Voronoi Block in the 3DEC software. Zhang et al. [9] applied a bonded model in PFC2D to study the stress and pore structure evolution characteristics of rock masses during compaction.

Extensive studies have been conducted on the deformation characteristics of rock masses, stress-time curves, and energy evolution under compression. The variation trends for a series of compaction parameters over time were derived. However, few studies deal with the strength parameters and mechanical behavior of the consolidated bodies. The mechanical properties of the consolidated bodies change considerably when compared to the intact rocks. It is important to understand the compaction and consolidation status and mechanical behaviors of the consolidated bodies. In this study, we first determine the mineral compositions and contents of mudstone and sandy mudstone using X-ray diffraction (XRD) and SEM. Thus, the microscopic morphologies of the two types of rocks were obtained. Subsequently, a self-developed compression testing apparatus was employed for orthogonally designed confined compression tests of the rock masses. In this way, we analyzed the influence of moisture content, compression ratio, particle size, and volume-based gradation of the rock masses on the compaction characteristics of the rock masses. The degrees of influence of each of the four factors on the stability of the consolidated bodies were determined. We further elucidated the influence mechanism of these four factors on the compressive and shear strengths of the consolidated bodies. A mathematical model was built for the mechanical behaviors of the consolidated bodies under the influence of the four factors.

2. Compression Test and Composition of Crushed Rock Masses

2.1. Sample Preparation and Test Design

2.1.1. Preparation of Crushed Rock Masses. The crushed rock mass samples were collected from the rocks surrounding the regenerated roof in the 1212 (3) slicing fully mechanized working face of Panbei Coal Mine in the Huainan mining area. The samples were primarily composed of mudstone and sandy mudstone. Large rock masses collected on site were first crushed using a crushing machine. Based on the grain size gradation of gangues in different areas in the direction of goaf inclination, through the similarity theory and Taibo theory, mudstones and sandy mudstones with four particle size gradations (<1 mm, 1–3 mm, 3–5 mm, and 5–10 mm) were obtained using a grading sieve. The four

Table 1: Factors and levels in orthogonal design.

Level	Factor			
	Moisture content	Compression ratio	Particle size	Volume-based gradation
1	5%	18% (24.3 mm)	≤1	Sandy mudstone
2	6%	21% (28.4 mm)	1-3	Mudstone
3	7%	27% (36.5 mm)	3-5	Sandy mudstone : mudstone = 2 : 1
4	8%	30% (40.5 mm)	5-10	Sandy mudstone : mudstone = 1 : 2

Table 2: Orthogonal design scheme.

Test	Moisture content	Compression	Particle size	Volume-based gradation
1	1	1	1	1
2	1	2	2	2
3	1	3	3	3
4	1	4	4	4
5	2	1	3	4
6	2	2	4	3
7	2	3	1	2
8	2	4	2	1
9	3	1	4	2
10	3	2	3	1
11	3	3	2	4
12	3	4	1	3
13	4	1	2	3
14	4	2	1	4
15	4	3	4	1
16	4	4	3	2

Note: the levels 1, 2, 3, and 4 assigned to the moisture content represent moisture content of 5%, 6%, 7%, and 8%, respectively. A similar design was adopted for the compression ratio, particle size, and volume-based gradation.

levels pertaining to the moisture content were 5%, 6%, 7%, and 8%, respectively.

2.1.2. Test Design. An orthogonal design was adopted to analyze the compaction characteristics of the crushed rock masses and the mechanical behaviors of the consolidated bodies. Four factors that influence the rock block compaction were chosen, namely, the moisture content, compression ratio, particle size, and volume-based degradation. Four levels were assigned to each factor to construct the orthogonal array L16 (45), as shown in Table 1. After the slice mining of the 1212 (3) fully mechanized working face, the mudstone and sandy mudstone layers in the direct roof collapsed. A bulking factor of 1.7 was chosen for the caving rocks [34]. The rock masses were compacted and consolidated under the load exerted by the overlying strata. Therefore, a residual bulking factor of 1.4 was chosen for the caving rocks [34]. The compression ratio of the caving rocks was estimated to be 17.6%. Based on the preliminary analysis, four levels were assigned to the compression ratio, namely, 18%, 21%, 27%, and 30%. The height of filled rock in the compression testing apparatus was 135 mm. Therefore, the corresponding compressions were 24.3 mm, 28.4 mm, 36.5 mm, and 40.5 mm. Based on the principles of orthogonal design, sixteen groups of tests were designed as shown in Table 2.

2.1.3. Testing Apparatus. The compression testing apparatus was made of high-strength steel, with an internal diameter of 50 mm and height of 140 mm. It had a double-open cylinder barrel, base, fastening ring, and compression head. The WAW-2000H computerized electrohydraulic servo universal testing machine was used for loading at a rate of 0.01 mm/s. The load was maintained constant for 5 min after reaching the specified level. A lubricant was applied to the inner wall of the double-open cylinder barrel to reduce the friction between the rock masses and the inner wall of the cylinder barrel. Based on the testing protocol, an appropriate quantity of crushed rock masses was weighed and stirred evenly. The rock masses were poured into the compression testing apparatus in batches and tamped down. After the test, the fastening ring was removed, and the double-open cylinder barrel was opened. The consolidated bodies were taken out and wrapped in film to retain their freshness.

The WAW-2000H Computerized Electro-hydraulic Servo Universal Testing Machine was used for the uniaxial compression test and shear test under displacement-controlled loading at a rate of 0.01 mm/s. For the shear test, three cylindrical dies having angles of 45°, 50°, and 55° with an internal diameter of 50 mm and height of 50 mm were designed and prepared. Before the test, lubricant was applied to the shear planes of the dies to reduce the friction between the upper and lower shear planes. A high-definition SLR digital camera was used to take a series of photographs of the uniaxial compression and shear failure of the consolidated bodies. The confined compression test of crushed rock masses and the uniaxial compression and shear tests of the consolidated bodies are illustrated in Figure 1.

During the shear test, the axial pressure P acting on the dies was decomposed into a normal stress N perpendicular to the shear plane and a tangential stress T parallel to the shear plane. The axial pressure acts uniformly on the shear plane of the dies. The area of the shear plane is denoted by F. The corresponding normal stress and shear stress are as follows:

$$\sigma = \frac{N}{F} = \frac{P}{F} \sin \alpha, \tag{1}$$

$$\tau = \frac{T}{F} = \frac{P}{F} \cos \alpha, \tag{2}$$

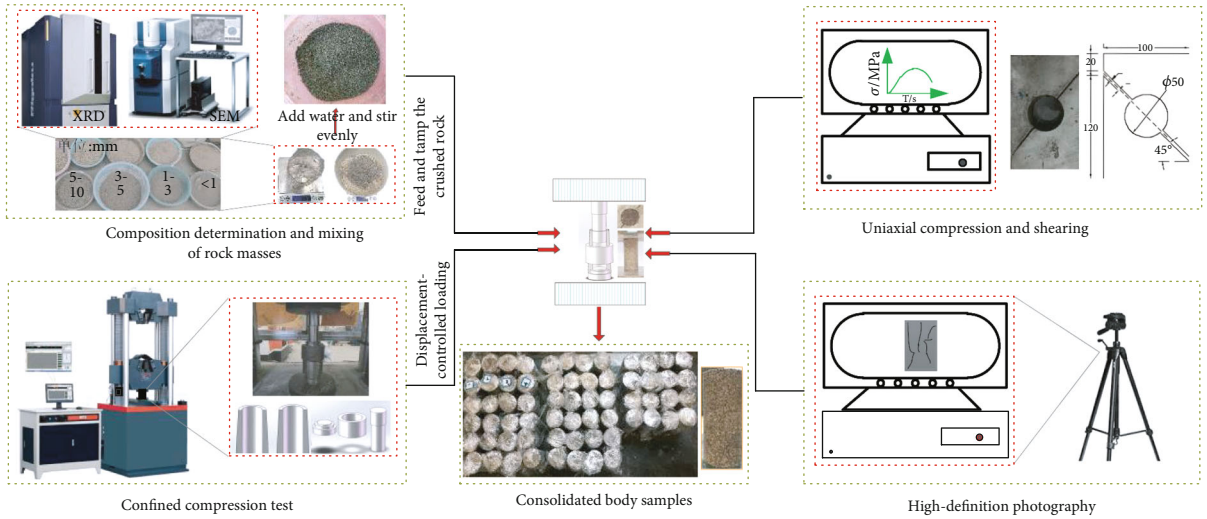

Figure 1: Test process.

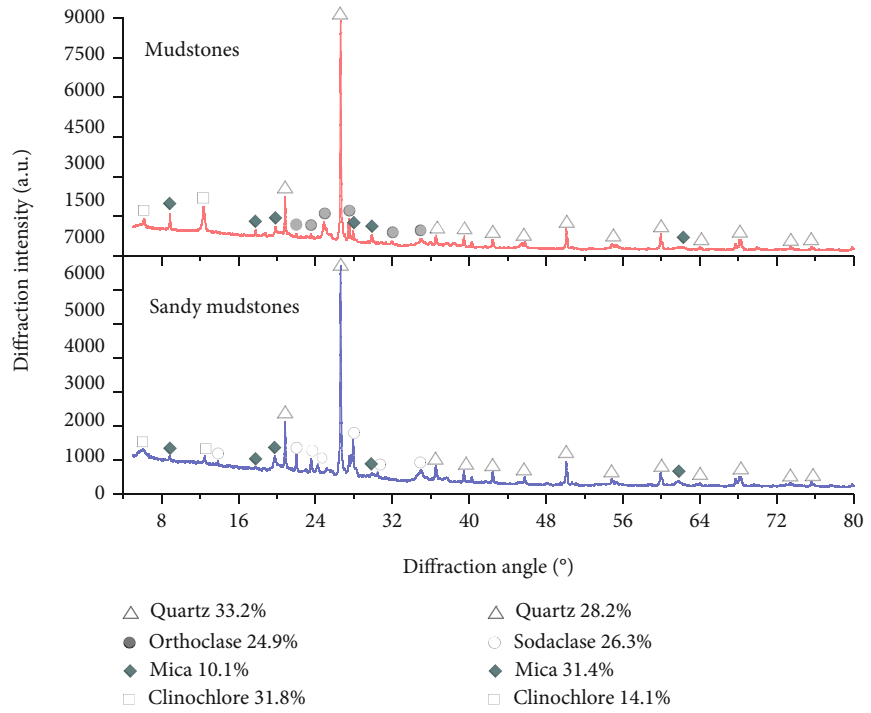

Figure 2: XRD spectra of crushed rock masses.

where F is the area of the shear plane, m^2; σ is the normal stress, MPa; τ is the shear stress, MPa; and α is the included angle between the shear plane of the dies and the horizontal plane, °.

The dies were used for the shear test. The normal and shear stresses corresponding to the three angles were estimated and plotted in the τ-σ Cartesian coordinate system. Data points for each group were connected into a curve, i.e., the shear strength curve of the rock masses. For ease of application, the above curve is usually simplified into a straight line, namely,

$$\tau = \sigma \tan \varphi + C, \tag{3}$$

where C is the intercept of the straight line on the y-axis (τ-axis), i.e., cohesion of the rock masses, MPa; φ is the included angle between the straight line and the x-axis (σ-axis), i.e., the internal friction angle of the rock masses, °.

2.2. Composition of Crushed Rock Masses. The XRD patterns of the crushed mudstones and sandy mudstones are shown in Figure 2. It can be seen from the figure that rocks of the two lithologies were both comprised of quartz, mica, and chlorite. The quartz content was 33.2% in the mudstones and 28.2% in the sandy mudstones. The quartz formed a solid skeleton in each. The chlorite content was 31.8% in the mudstones and 14.1% in the sandy mudstones.

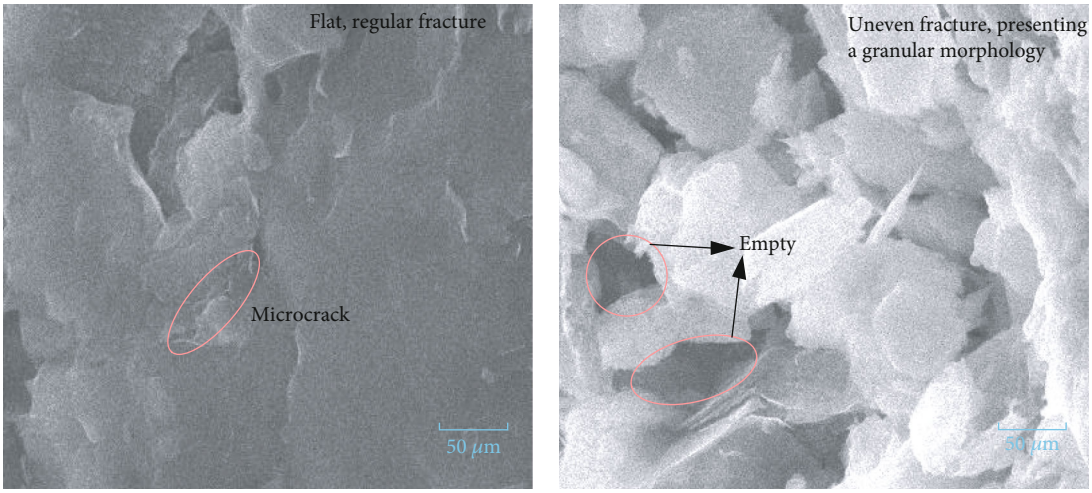

(a) Mudstones (b) Sandy mudstones

Figure 3: SEM patterns of crushed rock masses.

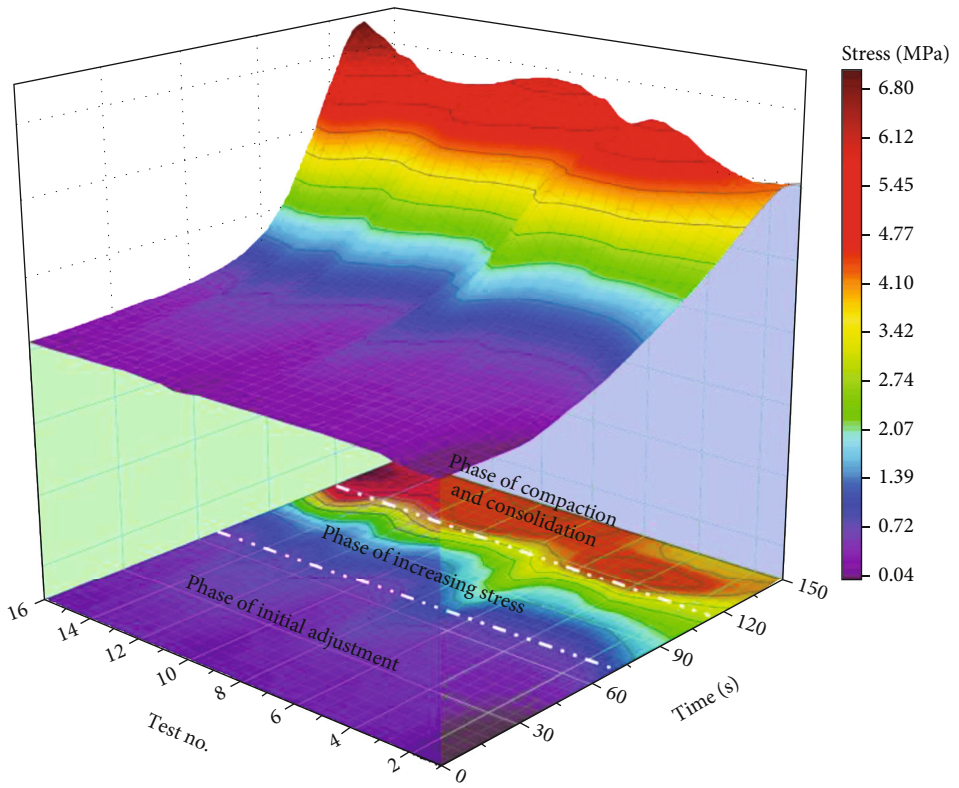

Figure 4: Consolidation stress-time curves of the crushed rock masses.

Therefore, the mudstones had a higher cementing ability than the sandy mudstones.

The microscopic structures of the crushed and sandy mudstones characterized by SEM are shown in Figure 3. It can be observed from the figure that the micropores were developed locally on the surface of the mudstones. A dense pelitic texture was observed for the flat fracture. The solid skeleton was formed by quartz and feldspar and filled with a large number of clay minerals. Micropores were developed on the surface of the sandy mudstones. The fracture was uneven, and sharp-edged quartz and feldspar particles of unequal sizes were distributed randomly on the surface, forming a porous, stacked, and loose solid skeleton. Scales of clay minerals could be found on the skeleton surface.

In general, mudstone and sandy mudstone are rich in cemented minerals such as quartz and chlorite, which is conducive to promoting the cemented regeneration of caving gangue in goaf. At the same time, it can provide basic data for the microanalysis of the strength characteristics of the consolidated body.

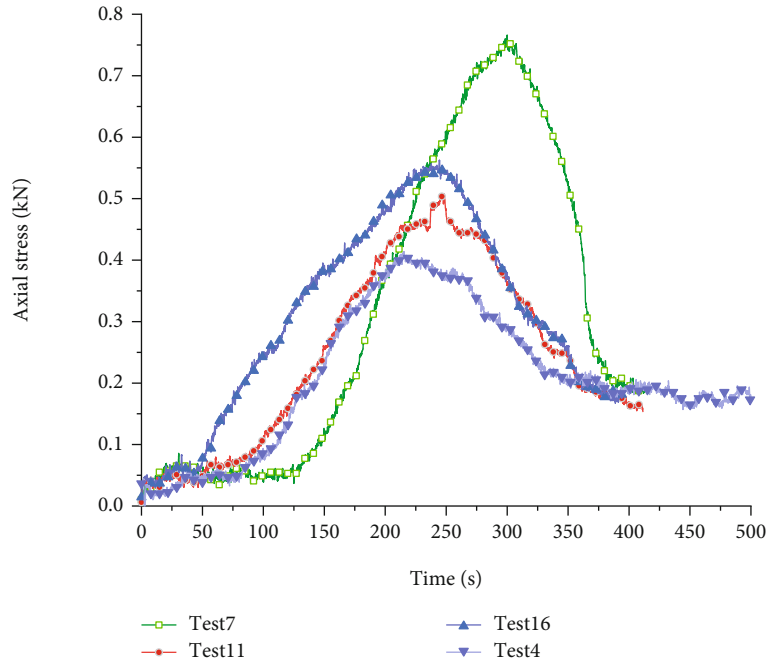

Figure 5: Uniaxial compressive stress-time curves of the crushed rock masses.

3. Results and Discussion

3.1. Consolidation Characteristics of Crushed Rock Masses. Typical data for the confined compression tests were chosen for crushed rock masses to estimate the compaction stress-time relationship, as shown in Figure 4. The compaction stress-time curve could be divided into three phases. The first phase was the initial adjustment phase, during which the compressive deformation increased. This phase was relatively long and was associated with a small compaction stress as the rock masses were loose at the beginning of compression. The edges and corners were sharper and there were larger gaps between the masses. The contact status of the rocks were adjusted constantly at this phase, although at a lower rate. As the compression proceeded, the rock masses became more compacted and got into closer contact with each other. Thus, the increasing stress phase began and proceeded at an accelerating rate. At this phase, the edges and corners of the rock masses compressed and squeezed each other, causing fracturing, breakage, and subsequent pulverization. The large gaps between the rock masses were filled with this powdered material, which changed the particle sizes and their spatial distribution. As a result, the contact between the rock masses got modified at an accelerating rate. A triaxial stress system was set up gradually, which was accompanied by an exponential growth in the compaction stress. As the compression proceeded further, the phase of compaction and consolidation became characterized by reduced deformation, shorter duration, and smaller changes in compaction stress. Finally, stable consolidated bodies were formed with coarse-grained rock masses as the skeleton and fine-grained rock masses occupying the spaces within.

3.2. Mechanical Behavior of Consolidated Bodies. Limited by the length of the article, only 16 groups of test data are selected to analyze the mechanical behavior of the consolidated bodies. The influence characteristics of compressibility, moisture content, and volume gradation on the uniaxial compressive strength and shear strength of the consolidated body can refer to the results of rock particle size analysis.

3.2.1. Uniaxial Compressive Strength. Typical data for uniaxial compression tests were chosen for the consolidated bodies to estimate the axial stress-time relationship and obtain the uniaxial compressive failure characteristics, as shown in Figures 5 and 6. It can be seen that the initial compression stage of the consolidated bodies lasted for a longer period of time as the consolidated bodies took less time to be molded by primary compaction. Due to the presence of water, the physical and chemical reactions between the rock masses were incomplete and the metamorphic effect was weak. The consolidated bodies were highly heterogeneous and had poor internal stability. Under secondary compression, the contact between the rock masses was enhanced, and the pores within the consolidated bodies were compressed. During this phase, the stress status evolved towards equilibrium. As the axial pressure increased, the consolidated bodies entered the energy storage phase. New cracks were initiated on the surface, and these propagated towards the two ends. Subsequently, the plastic failure phase commenced and was characterized by the significant stress fluctuation. When only the particle size of the rock masses were considered, the ductile failure characteristics changed from overall cracking with transverse and longitudinal crack development to expansion cracking with the propagation of irregular and dense cracks and, finally, to the bulging and shedding of rock particles.

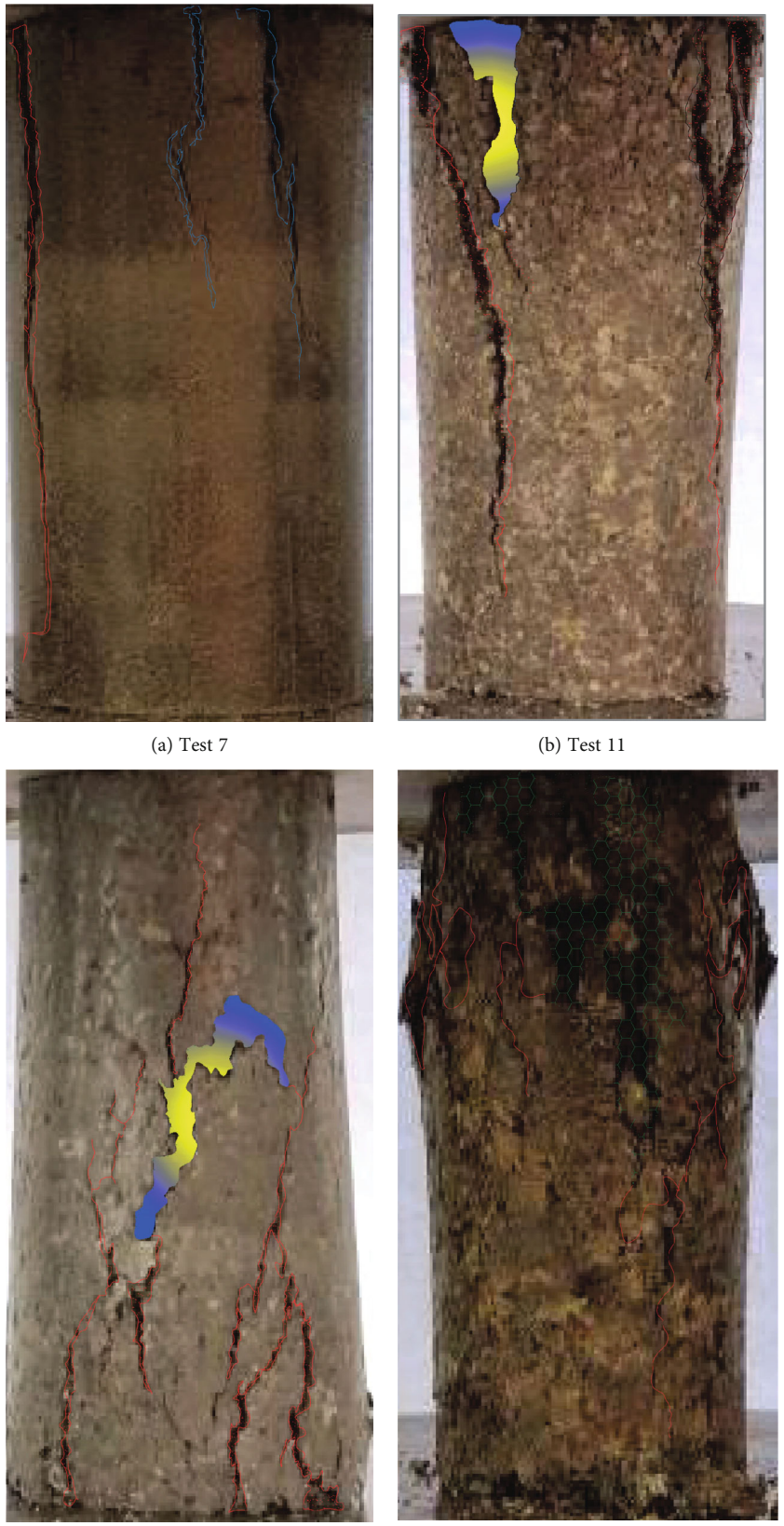

(a) Test 7

(b) Test 11

(c) Test 16

(d) Test 4

Figure 6: Uniaxial compression failure characteristics of the consolidated bodies.

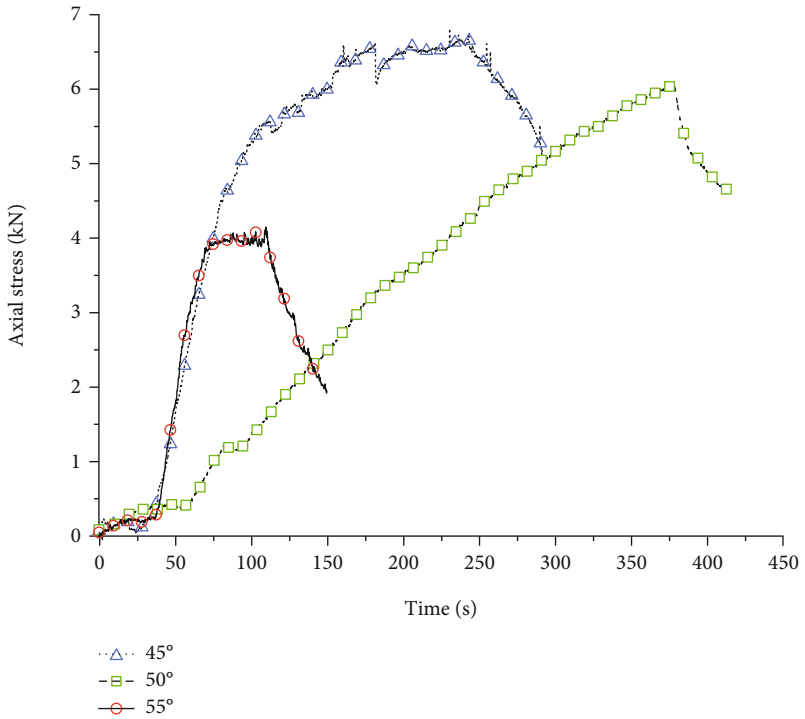

(a) Test 7

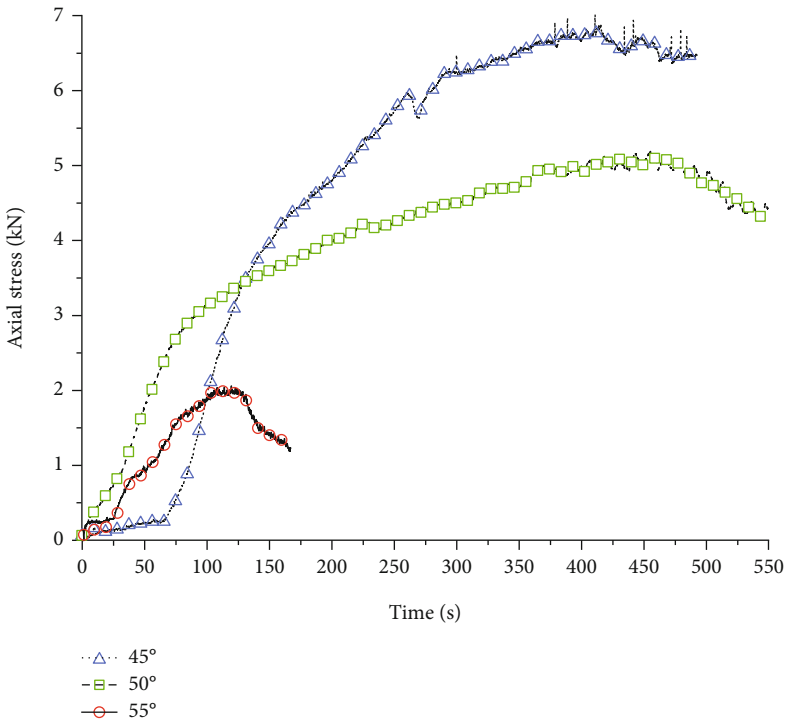

(b) Test 11

Figure 7: Continued.

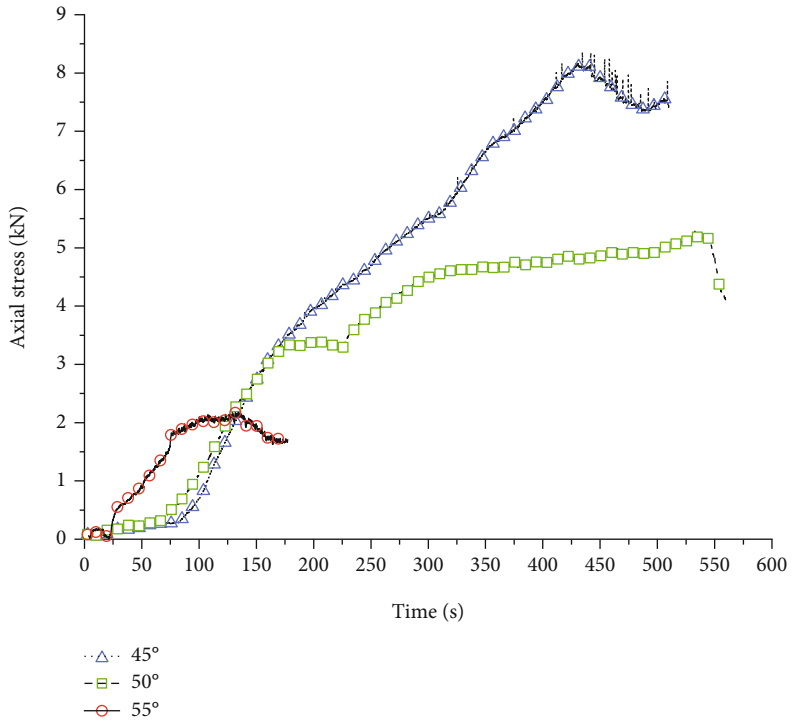

(c) Test 16

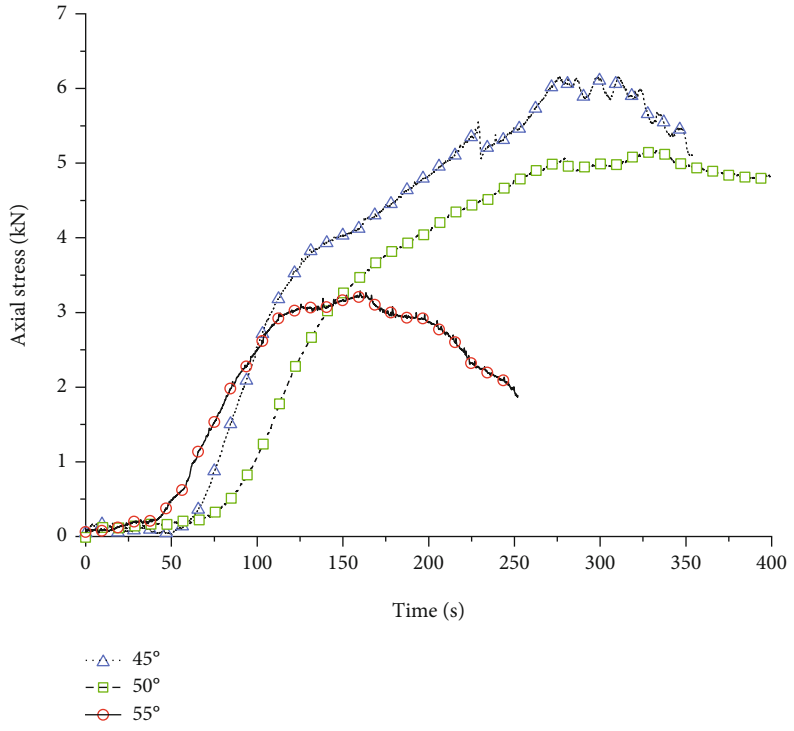

(d) Test 4

Figure 7: Shear axial pressure-time curve of secondary diagenesis specimen.

3.2.2. Shear Strength. According to the shear test data of typical consolidated secondary diagenesis specimens, the relationship between axial pressure and shear time is obtained, as shown in Figure 7. It can be seen that the shear axial pressure of the consolidated secondary diagenesis specimen is similar to the axial stress change of uniaxial compression, and both have the fluctuation of stress (pressure) change. At the initial stage of the shear test, the pressure fluctuation is not obvious, and the axial pressure increases linearly. At the stage of nonlinear increase of axial pressure, the pressure fluctuation begins to increase. At the later stage of yield failure, the variation of axial pressure is further enhanced.

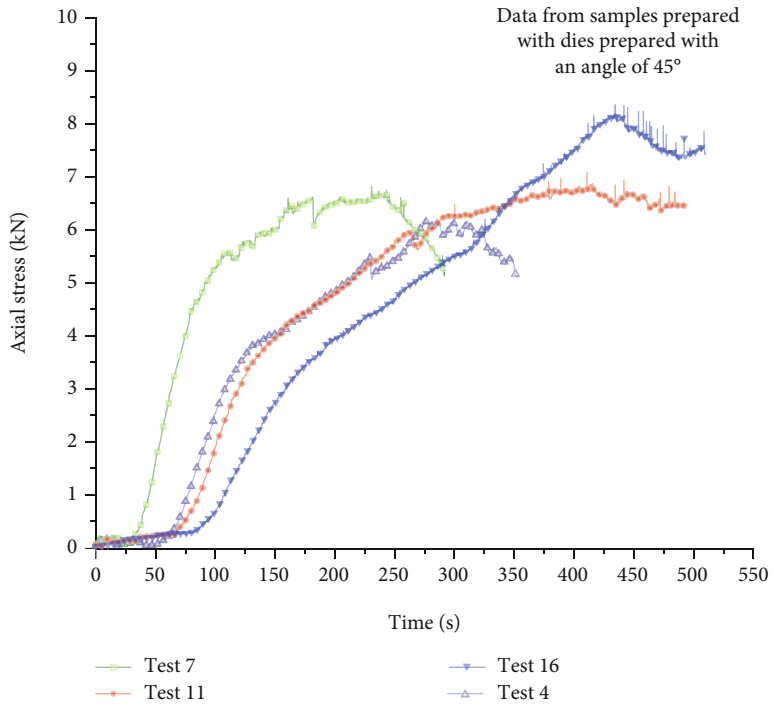

Figure 8: Shear stress-time curves.

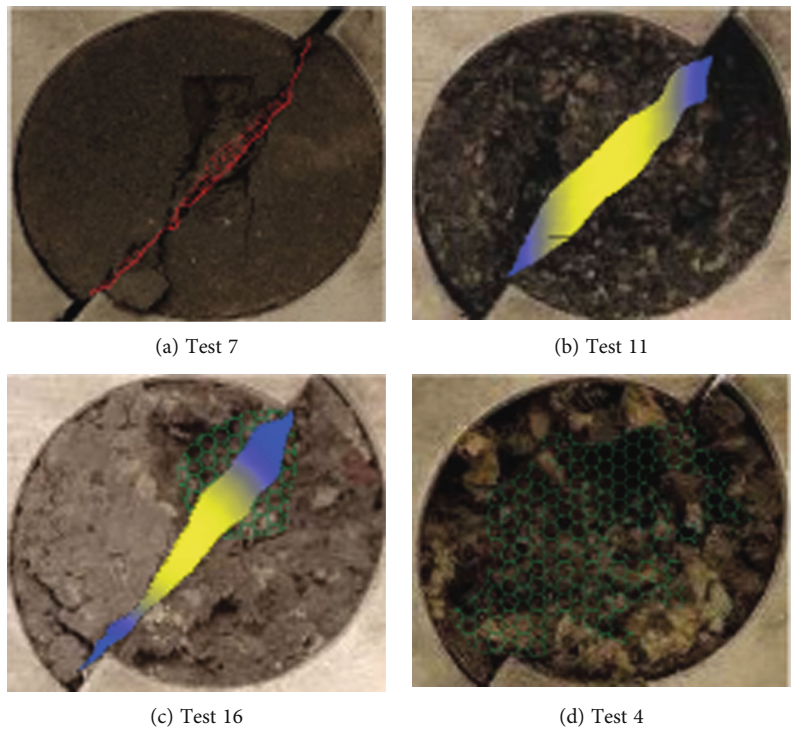

(a) Test 7 (b) Test 11

(c) Test 16 (d) Test 4

Figure 9: Shear failure characteristics of the consolidated bodies.

Typical shear test data were chosen for the samples prepared with the 45° die to estimate the axial stress-time relationship and obtain the shear failure characteristics, as shown in Figures 8 and 9. The axial pressure-time curves of the consolidated bodies during the shear tests were similar to the uniaxial compressive stress-time curves. However, during the energy storage stage of the consolidated bodies under shear, the changes in axial pressure were divided into two subphases, namely, linear energy storage and curved energy storage. When only the particle size of the rock masses was considered,

Table 3: Test results.

Test	Moisture content	Compression	Particle size	Volume-based gradation	Compaction stress (MPa)	Compressive strength (MPa)	Cohesion (MPa)	Internal friction angle (°)
1	1	1	1	1	4.348	0.423	0.175	31.65
2	1	2	2	2	4.107	0.463	0.154	39.27
3	1	3	3	3	4.174	0.471	0.147	38.41
4	1	4	4	4	6.162	0.614	0.310	34.64
5	2	1	3	4	2.244	0.185	0.088	42.12
6	2	2	4	3	2.350	0.180	0.094	40.55
7	2	3	1	2	6.043	0.767	0.396	31.75
8	2	4	2	1	5.703	0.558	0.145	28.09
9	3	1	4	2	1.704	0.167	0.147	42.11
10	3	2	3	1	1.781	0.210	0.132	35.82
11	3	3	2	4	5.613	0.508	0.151	41.35
12	3	4	1	3	5.945	0.689	0.291	36.87
13	4	1	2	3	2.289	0.340	0.104	41.35
14	4	2	1	4	3.940	0.428	0.154	40.62
15	4	3	4	1	2.785	0.434	0.160	41.43
16	4	4	3	2	6.978	0.563	0.119	42.26

Table 4: Ranges of influence factors of compaction stress.

Test	Range (MPa)
Moisture content	0.937
Compression ratio	3.551
Particle size	1.819
Volume-based gradation	1.054

the ductile failure characteristics underwent the following transition: cracks were first initiated and propagated along the shear plane in the consolidated bodies to form a shear line, followed by an irregular deformation along the shear plane to form a shear slot; finally, the rock masses became extruded and bulged out along the shear plane. These were later dislocated and fell off.

3.3. Range Analysis

3.3.1. Compaction Stress. The test results are obtained based on the 16 groups of tests in the orthogonal experiment table and Equations (1)–(3). Results of the compaction tests on crushed rock masses and the uniaxial compression tests and shear tests of the consolidated bodies are shown in Table 3.

The compaction stresses under the same level of each of the four influence factors were averaged. The ranges were calculated for each factor as shown in Table 4. Apparently, among the four influence factors, the range associated with the compression ratio was far greater than those of the other factors. This indicated that the compression ratio had the greatest influence on the compaction stress acting on the rock masses. In the descending order of the degree of influence on the compaction stress, the four influence factors were ranked as follows: compression ratio $(3.551) >$ particle size $(1.819) >$ volume − based gradation $(1.054) >$ moisture content (0.937).

The variation patterns of the compaction stress under different levels of the influence factors are shown in Figure 10. It can be seen from the figure that the compaction stress decreased significantly as the particle size increased. As shown above, the compaction of rock masses is a process where the contact and stress statuses change constantly. The gaps between the fine-grained rock masses were smaller. Therefore, the adjustment of the contact and stress statuses was faster under compression, and the increment of compaction stress needed for this process was also larger. However, for the coarse-grained rock masses, the compression caused the squeezing and fracturing of the edges and corners, and the rock masses were pulverized. The rounded coarse-grained rock masses interlocked with each other better to form a supportive skeleton. The rock powder migrated to and filled the gaps. However, there was not enough powder to fill all the gaps, which resulted in a lower degree of compaction of the consolidated bodies. For the same compaction history, the ultimate compaction stress needed for this process was lower.

The compaction stress increased significantly as the compression ratio increased. This is because, as the compression increased, the edges and corners of the rock masses were squeezed and fractured more, resulting in the formation of more powder. The degree of compaction of the rock masses also increased correspondingly. The contact and stress statuses were adjusted at an accelerating rate, resulting in a triaxial stress state being set up faster.

The compaction stress first decreased and then increased slightly as the moisture content increased as the rock masses were argillized upon contact with water. Under a lower axial pressure, the corners and edges of the rock masses were rounded due to fracturing and crushing. Under the same compression history, the compaction stress requirement for the above process was smaller. As the moisture content increased, the rock powder became more likely to migrate

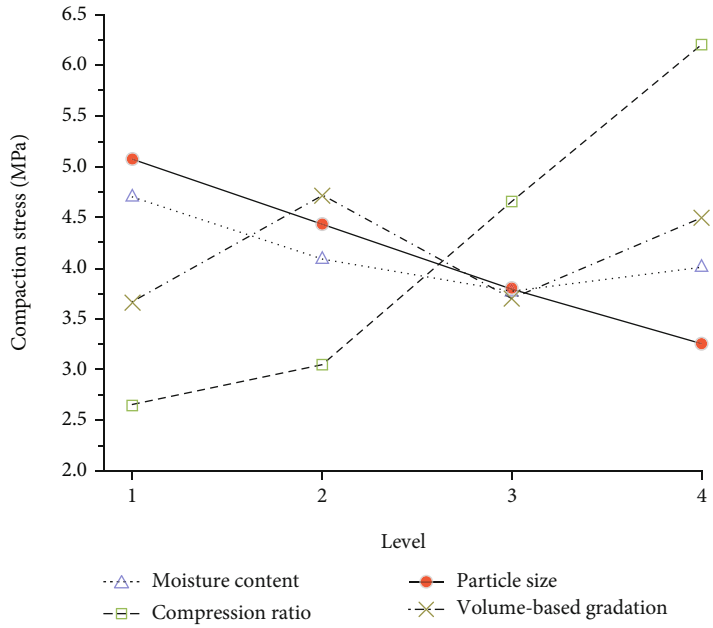

Figure 10: Sensitivity factor curves of the compaction stress.

Table 5: Ranges of the influence factors of compressive strength.

Test	Range (MPa)
Moisture content	0.099
Compression ratio	0.327
Particle size	0.220
Volume-based gradation	0.084

due to the edge effect of water, thus filling the gaps between the rock masses. This caused a slight increase in the compression stress. When the moisture content increased to a certain threshold, the rock powder flowed, making it more difficult for the rock masses to be compacted and molded.

3.3.2. Compressive Strength. The ranges of the four influence factors of compressive strengths of the consolidated samples are shown in Table 5. Apparently, among the four influence factors, the range was the largest for the compression ratio. This indicated that the compression ratio had the most significant influence on the compressive strength of the consolidated bodies. In descending order of the degree of influence on the compressive strength, the four influence factors were ranked as follows: compression ratio (0.327) > particle size (0.220) > moisture content (0.099) > volume − based gradation (0.084).

The variation patterns of the compressive strength under different levels of the four influence factors are shown in Figure 11. It can be seen that the compressive strength of the consolidated bodies decreases as the particle size increased. The degree of influence of the particle size on the compressive strength of the consolidated bodies varied for the fine- and coarse-grained rock masses: the fine-grained consolidated bodies resisted failure as a whole before uniaxial compressive failure occurred. The peak strength of the fine-grained consolidated bodies was determined by the strength of the rock masses. After the failure, macroscopic cracks were formed on the surface, which could be described as overall cracking. The particle size determined the degree of coarseness of the fracture surface. The compressive strength of the coarse-grained consolidated bodies was determined by the strength of the cemented surface between the rock masses. During uniaxial compression, failure first occurred on the cemented surface between the coarse-grained rock masses. Subsequently, the rock masses bulged out and fell off.

The compressive strength of the consolidated bodies increased as the compression ratio increased. This happened because the porosity of the consolidated bodies had a direct bearing on the compressive strength. Moreover, in practice, the caving gangues retained residual hulking after compression despite the considerable loads exerted by the overlying strata [34]. The axial pressure contributed to the compactness of the filling between the rock masses through the secondary crushing of the rock masses and adjustment of rock powder migration. As a result, the porosity of the consolidated bodies decreased, and the strength increased.

The compressive strength of the consolidated bodies first decreased and then increased slightly as the moisture content increased. Such variation was consistent with that observed during the compaction of the crushed rock masses. This variation could be explained in the same manner as above.

3.3.3. Tensile Strength. The ranges of the four influence factors on the cohesion and internal friction angle of the samples are shown in Table 6. It can be seen from here that, among the four influence factors, the range of the particle size was the largest. This indicated that the particle size had the greatest influence on the cohesion and internal friction angle of the consolidated samples. In the descending

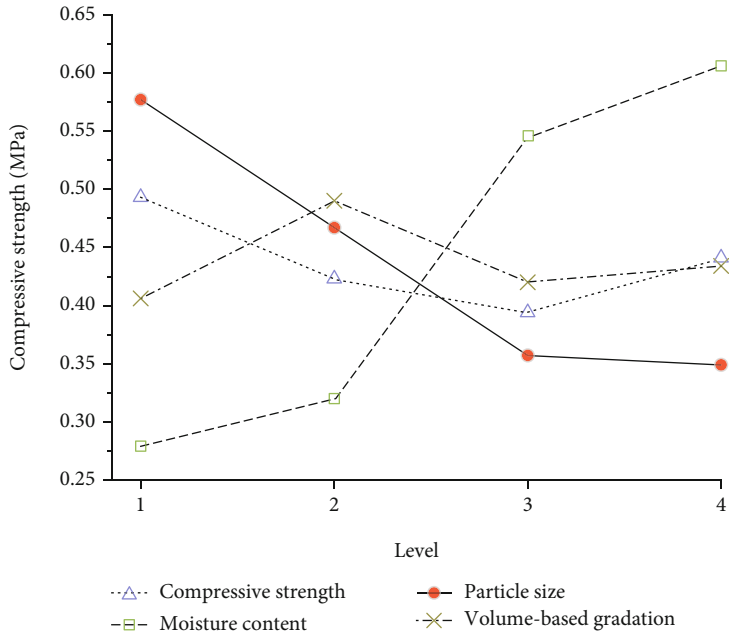

Figure 11: Sensitivity factor curves of the compressive stress.

Table 6: Ranges of the influence factors of cohesion and internal friction angle.

Test	Range (MPa)	Range (°)
Moisture content	0.063	3.19
Compression ratio	0.088	3.84
Particle size	0.132	4.46
Volume-based gradation	0.051	2.60

order of the degree of influence on the cohesion and internal friction angle, the four influence factors were ranked as follows: particle size (0.132/1.46) > compression ratio (0.088/3.84) > rate size > moisture content (0.063/3.19) > volume − based gradation (0.051/2.60).

The variations of the cohesion and internal friction angle under different levels of the four influence factors are shown in Figure 12. The cohesion of the consolidated bodies decreased as the particle size increased indicating an inverse relationship, while the internal friction angle showed a direct relationship. This was because the coarser the rock particles, the higher the degree of interlocking between the edges and corners would be. As a result, the shear resistance increased during the compression-shearing process, and the internal friction angle increased. However, the degree of bonding between the rock masses decreased, as did the cohesion.

The cohesion of the consolidated bodies increased as the particle compression ratio increased, indicating a direct relationship, while the internal friction angle varied inversely. This was because as the compression ratio increased uniformly, the edges and corners of the rock masses became squeezed and fractured. The coarse-grained rock masses became rounded, and the degree of interlocking between the rock masses decreased. The shear resistance of the consolidated bodies decreased, and the internal friction angle decreased as well. As the compaction ratio increased continuously, more rock powder filled the gap between the rock masses. The degree of bonding at the contact surfaces between the rock masses increased, as did the cohesion.

The cohesion of the consolidated bodies decreased as the particle size increased while variation of the internal friction angle showed a direct relationship. This was because at the initial stage of the compression-shearing process, the corners and edges of the rock masses underwent brittle failure. On contact with water, the corners and edges of the rock masses were argillized and underwent ductile failure. Therefore, the shear resistance and internal friction angles of the samples increased. As the moisture content increased, the rock powder showed an enhanced ability to migrate along the shear plane, which reduced the cohesion.

The degree of influence of volume-based gradation on the compaction stress of the crushed rock masses and compressive and shear strengths of the consolidated bodies was determined by the mineral composition of the rock masses.

3.4. Regression Model. In this paper, three factors and four levels of an orthogonal test scheme are selected, and there are many test results. Therefore, the response surface method in statistical analysis is used to carry out the regression analysis of test data with polynomial function. Based on the data from orthogonal array testing, the moisture content, compression ratio, particle size, and volume-based gradation were, respectively, set as independent variables denoted as x_1, x_2, x_3, and x_4. The compaction stress, compressive strength, cohesion, and internal friction angle were, respectively, set to be objective functions y_1, y_2, y_3, and y_4. Hence, a multiple nonlinear regression analysis was conducted, and the following regression

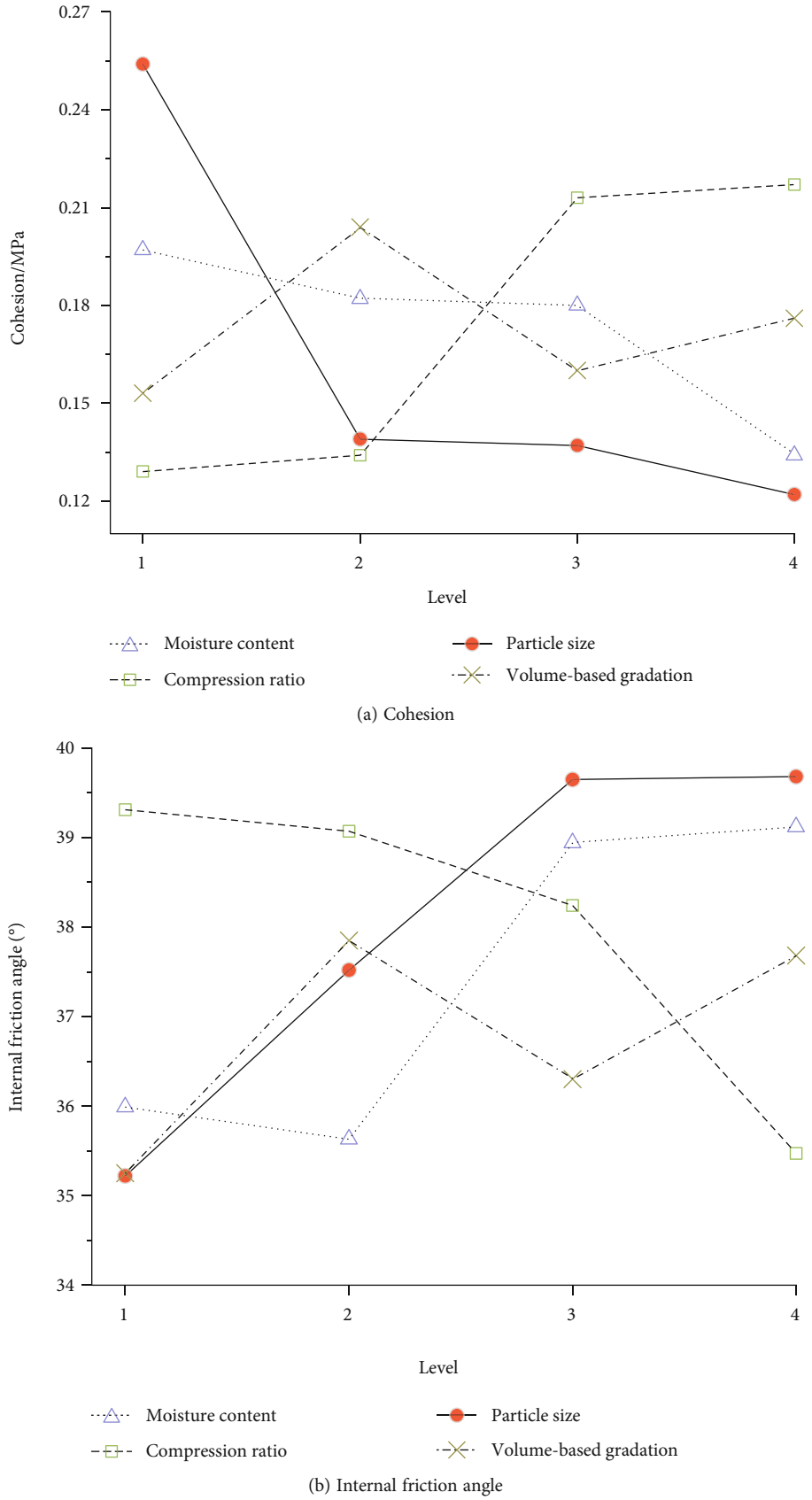

(a) Cohesion

(b) Internal friction angle

Figure 12: Sensitivity factor curves of the internal friction angle.

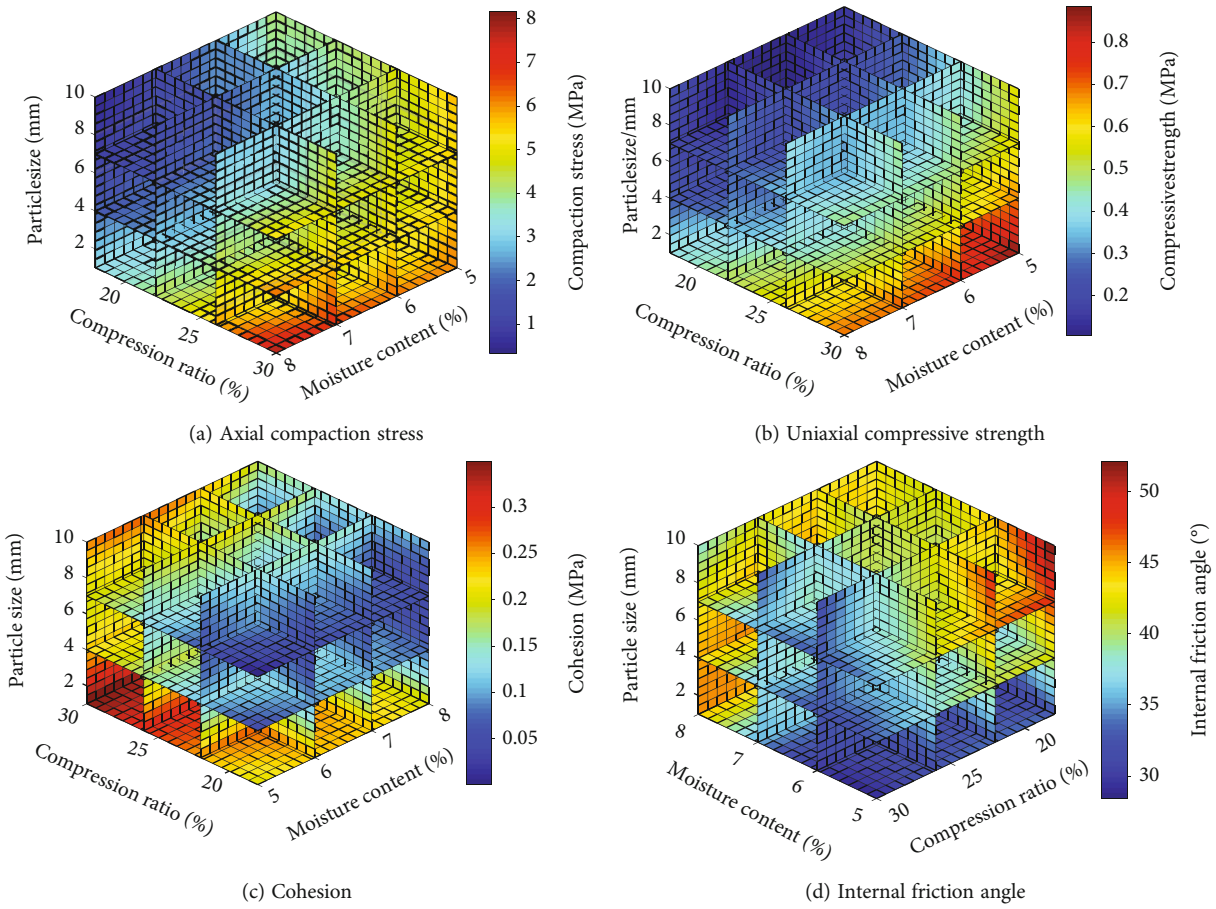

(a) Axial compaction stress

(b) Uniaxial compressive strength

(c) Cohesion

(d) Internal friction angle

Figure 13: Mathematical model of the objective function.

equations were obtained:

$$y_1 = 121.767 - 2999.090x_1 + 189.676x_2 - 1.307x_3 - 4.314x_4 + 159.752x_1x_2 + 22.074x_1x_3 + 18.229x_1x_4 - 11.087x_2x_3 - 1.316x_2x_4 + 0.531x_3x_4 + 15748.810{x_1}^2 - 267.393{x_2}^2 + 0.026{x_3}^2 + 0.810{x_4}^2, R_2 = 0.97, \quad (4)$$

$$y_2 = 1.049 - 45.733x_1 + 12.507x_2 - 0.336x_3 - 0.305x_4 - 59.094x_1x_2 + 2.008x_1x_3 - 2.898x_1x_4 - 0.020x_2x_3 + 0.037x_2x_4 + 0.017x_3x_4 + 317.102{x_1}^2 - 8.543{x_2}^2 + 0.006{x_3}^2 - 0.016{x_4}^2, R_2 = 0.98, \quad (5)$$

$$y_3 = 2.184 - 100.741x_1 + 18.524x_2 - 0.139x_3 + 0.494x_4 - 54.243x_1x_2 + 1.142x_1x_3 - 8.951x_1x_4 - 0.646x_2x_3 + 0.225x_2x_4 + 0.025x_3x_4 + 706.651{x_1}^2 - 22.711{x_2}^2 + 0.008{x_3}^2 + 0.042{x_4}^2, R_2 = 0.96, \quad (6)$$

$$y_4 = -1449.360 - 42699.900x_1 - 4285.301x_2 - 27.427x_3 - 52.726x_4 - 6818.473x_1x_2 - 289.662x_1x_3 - 1094.248x_1x_4 - 185.872x_2x_3 - 62.911x_2x_4 - 6.296x_3x_4 - 242890.300{x_1}^2 - 5619.939{x_2}^2 - 0.688{x_3}^2 - 17.0887{x_4}^2, R_2 = 0.99. \quad (7)$$

The regression models associated with the compaction stress, compressive strength, cohesion, and the internal friction angle were subject to 3D visualization. The functions of moisture content, compression ratio, and particle size as variables vs. different parameters were plotted in a 4D space, as shown in Figure 13. The smaller the particle size, the higher the water content, and the greater the compressibility, the greater the axial compaction stress required for rock compaction. The smaller the particle size, the smaller the water content, and the larger the compression ratio, the greater the uniaxial compressive strength and cohesion of the consolidated bodies. The larger the particle size and the smaller the water content, the compressibility of the consolidated bodies will be smaller, and the internal friction angle will be larger. The results from the prediction model were consistent with those from range analysis. Considering compressive strength as an example, the compressive strength of the consolidated bodies reached the maximum

when the particle size was below 1 mm, the compression ratio was 30%, and the moisture content was 5%. It should be noted that the relationship between the strength of the consolidated body and water content, compaction stress, and particle size is obtained within the test scope of this paper. In fact, under the same other conditions, there should be an optimal value of water content. When the compaction stress increases to a certain extent, the reduction of voids in compacted specimens is limited. The influence of particle size on secondary diagenesis is also related to the test scale and the content of fine materials and bonding materials. These related contents need to be further studied. At the same time, there are also great differences in mechanical behavior between consolidated body and rock mass. It is mainly due to the compaction and consolidation of the consolidated diagenetic specimen in a short time. The internal structure of the specimen is unstable without long-term metamorphism. The stress-strain curve of the consolidated body shows obvious heterogeneity. The strength of the consolidated body is affected by many factors, and the strength is low. Detailed soft rock support measures should be developed during the excavation of the project.

4. Conclusion

(1) Mudstones and sandy mudstones are rich in clay minerals, which contributes to the consolidation of the crushed rock masses and secondary diagenesis. The compression process of the rock masses can be divided into three phases, namely, the initial adjustment phase, the stress increase phase, and the compaction and consolidation phase

(2) The stress (pressure) increment was smaller and lasted for a longer period of time during the initial stage of the uniaxial compression and compaction-shearing process. The stress fluctuated more dramatically at the plastic failure stage, resulting in ductile failure

(3) The essence of crushed rock block compression is the process of continuous adjustment of contact state and stress state between rock blocks. The greater the compressibility, the higher the degree of angular crushing of rock blocks, the faster the migration of fine-grained rock blocks, and the denser the interstices between rock blocks. The finer the particle size of the rock block, the smaller the gap between the rock blocks. Under the high compression rate, the adjustment speed of the contact state and stress state between the rock blocks is accelerated, and the rock blocks enter the triaxial stress state faster. When the water content is at a low level, the water mainly softens the edges and corners of rock blocks. With the increase of water content, the water wedge effect is enhanced, and the fine-grained rock blocks are easier to move and adjust

(4) The compression ratio and particle size were the most important influence factors of the compressive and shear strengths of the consolidated bodies. The compression ratio influenced the porosity of the consolidated bodies as well as the degree of interlocking and bonding of the edges and corners. The particle size affected the failure mode of the consolidated bodies and the degree of interlocking and bonding of the edges and corners

(5) Based on the data from orthogonal array tests, we built a multiple nonlinear regression model. The degrees of influence of the moisture content, compression rate, and particle size were visualized in 3D. Thus, the compaction characteristics of the crushed rock masses and the mechanical behaviors of the consolidated bodies under the influence of each factor were elucidated and presented in an intuitive format

Data Availability

The data used for conducting classifications are available from the corresponding author upon request.

Conflicts of Interest

The authors declare that they have no conflicts of interest.

Acknowledgments

This work was supported by the Key Project Natural Science Research of Anhui Universities (No. KJ2021A0456), the Introduction of Talents Research Project of Anhui University of Science and Technology (No. 2021YJRC10), the Key Project of the National Natural Science Foundation of China (No. 51634007), the Graduate Innovation Fund Project of the Anhui University of Science and Technology of China (2020CX1002), and the Major Special Projects of Science and Technology in Shanxi Province (No. 20191101016).

References

[1] W. Q. Ma and T. X. Wang, "Instability mechanism and control countermeasure of a cataclastic roadway regenerated roof in the extraction of the remaining mineral resources: a case study," *Rock Mechanics and Rock Engineering*, vol. 52, no. 7, pp. 2437–2457, 2019.

[2] C. Xiao-lou, L. Qin-jie, Y. Ke et al., "Cataclastic regenerated roof and instability mechanism of support in fully mechanized mining face of steeply dipping seam," *Journal of China Coal Society*, vol. 45, no. 9, pp. 3045–3053, 2020.

[3] K. Yang, X. Chi, W. Liu, L. Dou, and Z. Wei, "Strong ground pressure mechanism and control at the longwall top coal caving with a single key stratum in goaf," *Shock and Vibration*, vol. 2020, 12 pages, 2020.

[4] C. Zhang, S. H. Tu, and Y. X. Zhao, "Compaction characteristics of the caving zone in a longwall goaf: a review," *Environmental Earth Sciences*, vol. 78, no. 1, pp. 27–42, 2019.

[5] J. Zhang, Q. Zhang, Q. Sun, R. Gao, D. Germain, and S. Abro, "Surface subsidence control theory and application to backfill coal mining technology," *Environmental Earth Sciences*, vol. 74, no. 2, pp. 1439–1448, 2015.

[6] N. Zhou, X. Han, J. Zhang, and M. Li, "Compressive deformation and energy dissipation of crushed coal gangue," *Powder Technology*, vol. 297, pp. 220–228, 2016.

[7] D. L. Yang, J. P. Li, C. L. Du, K. H. Zheng, and S. Y. Liu, "Particle size distribution of coal and gangue after impact-crush separation," *Journal of Central South University*, vol. 24, no. 6, pp. 1252–1262, 2017.

[8] J. Li, Y. Huang, Z. Chen, J. Zhang, H. Jiang, and Y. Zhang, "Characterizations of macroscopic deformation and particle crushing of crushed gangue particle material under cyclic loading: in solid backfilling coal mining," *Powder Technology*, vol. 343, pp. 159–169, 2019.

[9] C. Zhang, J. Liu, Y. Zhao, P. Han, and L. Zhang, "Numerical simulation of broken coal strength influence on compaction characteristics in goaf," *Natural Resources Research*, vol. 29, no. 4, pp. 2495–2511, 2020.

[10] C. Zhang, Y. Zhao, and Q. Bai, "3D DEM method for compaction and breakage characteristics simulation of broken rock mass in goaf," *Acta Geotechnica*, vol. 17, no. 7, pp. 2765–2781, 2022.

[11] J. Zhang, M. Li, Z. Liu, and N. Zhou, "Fractal characteristics of crushed particles of coal gangue under compaction," *Powder Technology*, vol. 305, pp. 12–18, 2017.

[12] D. M. Pappas and C. Mark, "Load deformation behavior of simulated longwall gob material," in *Proceedings of the 12th International Conference on Ground Control in Mining*, pp. 184–193, Morgantown, WV: West Virginia University, 1993.

[13] D. Ma, H. Bai, X. Miao, H. Pu, B. Jiang, and Z. Chen, "Compaction and seepage properties of crushed limestone particle mixture: an experimental investigation for Ordovician karst collapse pillar groundwater inrush," *Environmental Earth Sciences*, vol. 75, no. 1, p. 11, 2016.

[14] H. Bing-nan and G. Ai-guo, "Testing study on coal waste backfilling material compressiongs simulation," *Journal of China Coal Society*, vol. 34, no. 8, pp. 1076–1080, 2009.

[15] Y. L. Huang, J. M. Li, D. Ma, H. Gao, Y. Guo, and S. Ouyang, "Triaxial compression behaviour of gangue solid wastes under effects of particle size and confining pressure," *Science of the Total Environment*, vol. 693, no. 25, article 133607, 2019.

[16] Y. X. Guo, H. Y. Ran, G. R. Feng, X. J. du, T. Y. Qi, and Z. H. Wang, "Effects of curing under step-by-step load on mechanical and deformation properties of cemented gangue backfill column," *Journal of Central South University*, vol. 27, no. 11, pp. 3417–3435, 2020.

[17] L. Meng, Z. Jixiong, and G. Rui, "Mechanical analysis of roof subsidence based on rheological properties of solid backfill materials," *Teh vjesn*, vol. 25, no. 1, pp. 152–157, 2018.

[18] C. D. Su, M. Gu, X. Tang, and W. B. Guo, "Experiment study of compaction characteristics of crushed stones from coal seam roof," *Chinese Journal of Rock Mechanics and Engineering*, vol. 31, no. 1, pp. 18–26, 2012.

[19] L. Zhan, Z. Nan, and Z. Jixiong, "Random gravel model and particle flow based numerical biaxial test of solid backfill materials," *Mining Science and Technology*, vol. 23, no. 4, pp. 463–467, 2013.

[20] Y. Bang-yong, C. Zhan-qing, W. Jiang-yu, L. Qiang, and D. Qile, "Experimental study of compaction and fractal properties of grain size distribution of saturated crushed mudstone with different gradations," *Rock and Soil Mechanics*, vol. 37, no. 7, pp. 1887–1894, 2016.

[21] Z. G. Ma, T. Lan, Y. G. Pan, J. G. Ma, and F. H. Zhu, "Experimental study on variation law of saturated broken mudstone porosity during creep process," *Chinese Journal of Rock Mechanics and Engineering*, vol. 28, no. 7, pp. 1447–1454, 2009.

[22] J. W. Zhang, H. L. Wang, S. J. Chen, and Y. L. Li, "Bearing deformation characteristics of large-size broken rock," *Journal of China Coal Society*, vol. 43, no. 4, pp. 1000–1007, 2018.

[23] J. Zhenquan, J. Liangjun, and Z. Rusong, "Research on mechanism of crushing-compression of coal waste," *Journal of China University of Mining & Technology*, vol. 30, no. 2, pp. 139–142, 2001.

[24] Z. Zhennan, M. Xiexing, and G. Xiurun, "Testing study on compaction breakage of loose rock blocks," *Chinese Journal of Rock Mechanics and Engineering*, vol. 24, no. 3, pp. 451–455, 2005.

[25] Y. Xiao, H. Liu, Y. Chen, and J. Chu, "Influence of intermediate principal stress on the strength and dilatancy behavior of rockfill material," *Journal of Geotechnical & Geoenvironmental Engineering*, vol. 140, no. 11, pp. 1–15, 2014.

[26] L. Yimin, L. Huabei, and M. Haijun, "DEM investigation of the effect of intermediate principle stress on particle breakage of granular materials," *Computers and Geotechnics*, vol. 84, pp. 58–67, 2017.

[27] C. Wang, Y. Lu, Y. Li, B. Zhang, and Y. Liang, "Deformation process and prediction of filling gangue: a case study in China," *Geomechanics & Engineering*, vol. 18, no. 4, pp. 1350–1357, 2019.

[28] M. Li, J. X. Zhang, and X. X. Miao, "Experimental investigation on compaction properties of solid backfill materials," *Mining Technology*, vol. 123, no. 4, pp. 193–198, 2014.

[29] Y. H. Cheng, X. S. Guo, F. X. Jiang, and Z. L. Fu, "Experimental study and application of the different waste rock compaction characteristics filled in roadside of gob-side entry retaining," *Advanced Materials Research*, vol. 356-360, no. 360, pp. 2725–2729, 2011.

[30] W. Mingli, "Particle flow simulation of coal gangue compression test," *Chinese Journal of Rock Mechanics and Engineering*, vol. 32, no. 7, pp. 1350–1357, 2013.

[31] L. Huaiting, L. Junmeng, H. Yanli, S. Tianqi, K. Guoqiang, and W. Fengwan, "Macro-meso mechanical properties of waste discharged from open pit mine under triaxial compression," *Journal of Mining & Safety Engineering*, vol. 35, no. 1, pp. 170–178, 2018.

[32] C. Shugang, Z. Shi, L. I. Guodong, and C. Ran, "Experimental study on the bearing properties of granular gangue," *Chinese Journal of Underground Space and Engineering*, vol. 12, no. 5, pp. 1164–1171, 2016.

[33] Z. De-fu, T. Shi-hao, Y. Yong, M. Hang-sheng, and L. Xiang-yang, "An approach to determine the compaction characteristics of fractured rock by 3D discrete element method," *Rock and Soil Mechanics*, vol. 39, no. 3, pp. 1047–1055, 2018.

[34] Q. Ming-gao and X. Jia-lin, "Behaviors of strata movement in coal mining," *Journal of China Coal Society*, vol. 44, no. 4, pp. 973–984, 2019.